Chemical Science

ROYAL SOCIETY OF CHEMISTRY

EDGE ARTICLE

View Article Online
View Journal | View Issue

Check for updates

Cite this: *Chem. Sci.*, 2020, **11**, 4119

All publication charges for this article have been paid for by the Royal Society of Chemistry

Trends in C–O and N–O bond scission on rutile oxides described using oxygen vacancy formation energies†

Hai-Yan Su, [ab] Xiufang Ma, [c] Keju Sun,*[d] Chenghua Sun, [ae] Yongjun Xu[a] and Federico Calle-Vallejo *[f]

Received 29th January 2020
Accepted 20th March 2020

DOI: 10.1039/d0sc00534g

rsc.li/chemical-science

Reactivity trends on transition metals can generally be understood through the d-band model, but no analogous theory exists for transition metal oxides. This limits the generality of analyses in oxide-based catalysis and surface chemistry and has motivated the appearance of numerous descriptors. Here we show that oxygen vacancy formation energy (ΔE_{Vac}) is an inexpensive yet accurate and general descriptor for trends in transition-state energies, which are usually difficult to assess. For rutile-type oxides (MO_2 with M = 3d metals from Ti to Ni), we show that ΔE_{Vac} captures the trends in C–O and N–O bond scission of CO_2, CH_3OH, N_2O, and NH_2OH at oxygen vacancies. The proportionality between ΔE_{Vac} and transition-state energies is rationalized by analyzing the oxygen–metal bonds, which change from ionic to covalent from TiO_2 to NiO_2. ΔE_{Vac} may be used to design oxide catalysts, in particular those where lattice oxygen and/or oxygen vacancies participate in the catalytic cycles.

1. Introduction

With the advent and increase in the use of Density Functional Theory (DFT), the theoretical description of catalytic reactions has experienced great advances.[1–3] The properties at the atomic scale that determine the macroscopic kinetics have been established in numerous cases and some key descriptors, such as adsorption energies of intermediates,[1,4] band centers,[1] and coordination numbers,[5,6] among others,[7] have been identified to correlate with the catalytic activity. All this has substantially facilitated the rapid screening and *in silico* design of a large number of new materials.

However, the advancements pertain mostly to metals and many fundamental properties of the surfaces of metal oxides are still poorly understood due to their inherent complexity. This is because oxide properties depend on the interplay between the geometric structure, the band structure, the local stoichiometry of the surface and the oxidation states of the components.[8] In this context, a great challenge is the elaboration of an atomic-scale surface chemistry theory for metal oxides[3,9] as comprehensive as the d-band model for transition metals.[1] Such a theory would undoubtedly be the groundwork for the rational design of metal oxide catalysts.

Numerous studies have been conducted to identify the key factors that affect the activity of oxide surfaces. For instance, Shao-Horn *et al.* showed that the oxygen evolution activity of perovskite oxides exhibits a volcano-shaped dependence on the occupancy of the e_g orbitals, with the peak activity achieved at an e_g occupancy close to unity.[10] Similarly, Rossmeisl *et al.* proposed the concept of outer electrons to capture the trends in adsorption energies of metals, rock-salt monoxides, and perovskites altogether.[11] Jiang *et al.* proposed an adjusted coordination number as a general descriptor for the H adsorption energy and C–H activation energies over surface facets and defects of V_2O_3, Cr_2O_3, Co_3O_4, and NiO.[12] Furthermore, Morgan *et al.* reported that the experimentally measured area specific resistance and oxygen surface exchange of perovskites are well correlated with the DFT-calculated oxygen p-band center and vacancy formation energy.[13] Similarly, Dickens *et al.* reported a correlation between the average energy of adsorbed oxygens' 2p states and their reactivity at transition metals and some oxides.[14] Hinuma *et al.* also reported fair correlations

[a]School of Chemical Engineering and Energy Technology, Dongguan University of Technology, Dongguan, 523808, China
[b]State Key Laboratory of Molecular Reaction Dynamics, Dalian Institute of Chemical Physics, Chinese Academy of Science, Dalian, 116023, China
[c]Shenzhen Key Laboratory of Advanced Thin Films and Applications, College of Physics and Optoelectronic Engineering, Shenzhen University, Shenzhen, 518060, China
[d]Key Laboratory of Applied Chemistry, College of Environmental and Chemical Engineering, Yanshan University, 438 Hebei Avenue, Qinhuangdao, 066004, China. E-mail: kjsun@ysu.edu.cn
[e]Centre for Translational Atomaterials, Swinburne University of Technology, Hawthorn, Victoria 3122, Australia
[f]Departament de Ciència de Materials i Química Física, Institut de Química Teòrica i Computacional (IQTCUB), Universitat de Barcelona, Martí i Franquès 1, 08028 Barcelona, Spain. E-mail: f.calle.vallejo@ub.edu

† Electronic supplementary information (ESI) available: Lattice constants, adsorption energies and geometric data of intermediates, +U and dispersion tests, energetics and geometric configuration of C–O and N–O bond scission, and vacancy formation energies. See DOI: 10.1039/d0sc00534g

between oxygen vacancy formation energies and various adsorption energies.[15]

In addition, the versatile Brønsted–Evans–Polanyi (BEP) relation observed on metals is often found on rutiles and perovskites. This relation, which correlates elementary reaction thermodynamics and kinetics, seems to be universal on metals[16,17] but not on oxides, as it depends on the type of oxide, the active site and the dissociating molecules.[18]

Since the structural complexity of oxides appears to prevent the elaboration of universal descriptors, a viable strategy is to establish links between macroscopic functionality and atomic-scale properties for a given family of oxides.

The rutile TiO_2(110) surface is considered a prototypical system for metal oxide surfaces because of its rich surface chemistry and numerous applications in heterogeneous catalysis, photocatalysis, and gas sensors.[19–22] The surface reactivity of TiO_2(110) has been shown to be mainly controlled by defects, particularly oxygen vacancies.[23] The latter can either modify the behavior of neighboring metal sites or themselves act as active sites for many surface reactions, such as water dissociation and CO oxidation.[24–27] Other rutile oxides such as SnO_2, CeO_2, IrO_2, RuO_2 and MnO_2 have interesting applications in (electro)catalysis and gas sensing.[28–35] It has been argued that lattice oxygen may play a central role in the catalytic properties of some oxides,[36–41] typically *via* Mars/van Krevelen mechanisms in which oxygen vacancies are generated after lattice oxygen combines with reactants and/or intermediates.[42] Therefore, it is crucial to understand how oxygen vacancies affect the adsorption properties and catalytic activity of rutile oxide surfaces.

Using C–O and N–O bond scission in CO_2, CH_3OH, N_2O and NH_2OH as probe reactions, we show here that oxygen vacancy formation energy is a simple and robust descriptor for the bond-scission kinetics at oxygen vacancies of rutile-type MO_2(110) (M = 3d metals from Ti to Ni) surfaces. The results are useful for catalytic reduction of greenhouse gases such as N_2O[43] and CO_2,[44,45] CH_3OH photocatalytic oxidation,[46] and NH_2OH electrochemistry.[47]

Our results allow linking the adsorption energies of stationary and saddle points, which are difficult or currently impossible to measure[48] and tedious to calculate, to a single, computable and experimentally available descriptor for numerous oxide materials, namely oxygen vacancy formation energies. This can potentially streamline the fundamental understanding and rational design of oxide catalysts.

2. Methods

Spin-unrestricted DFT calculations were performed using the VASP[49] with PBE.[50] The interaction between the ionic cores and electrons was described by the projector-augmented wave (PAW) method,[51] and the Kohn–Sham valence electronic wave function was expanded in a plane-wave basis set with a kinetic energy cutoff of 400 eV. (2×1) 4-layer (110) slabs for MO_2 rutile oxides were used, separated by 15 Å of vacuum. The two bottommost layers were fixed at the bulk distances, and the two topmost layers and the adsorbates were fully relaxed. The Brillouin zones were sampled with $6 \times 4 \times 1$ Monkhorst–Pack grids.[52] The calculated lattice constants of the MO_2 oxides fall in the regions 4.31 Å $\leq a \leq$ 4.67 Å and 2.80 Å $\leq c \leq$ 2.97 Å, which agree well with the experimental values, as listed in Table S1.† The adsorption energy (ΔE_{Ads}) was calculated using the most stable configurations ($E_{MO_{2-v}+moiety}$) relative to the clean surfaces ($E_{MO_{2-v}}$) and the isolated molecules or their scission moieties (E_{moiety}):

$$\Delta E_{Ads} = E_{MO_{2-v}+moiety} - E_{MO_{2-v}} - E_{moiety} \quad (1)$$

where moiety = CO_2, CO, N_2, N_2O, CH_3OH, CH_3, OH, NH_2OH, NH_2, and $\frac{1}{2}O_2$. We calculated the adsorption energies of oxygen at the bridge oxygen vacancy on the MO_2(110) surfaces using DFT + U and found that the use of U does not alter the trends for oxygen adsorption, see Fig. S1a.† We also performed single-point DFT + U calculations for the activation energies and reaction energies of CO_2 and N_2O decomposition. Fig. S2† shows that the relationship between thermodynamics and kinetics also remains linear. Since we mainly focus on the trends in the present work, U was not included in the analysis.

We have also considered the effect of dispersion corrections for the particular case of $\Delta E_{Ads}(CO_2)$.[53] It can be seen from Table S2 and Fig. S1b† that the corrections only shift the adsorption energies downwards by 0.19 eV on average, without altering the overall trend.

Enthalpy changes (ΔH) are usually approximated as: $\Delta H \approx \Delta E + \Delta ZPE$ (ZPE: zero-point energy). For adsorbate *AB, one has: $ZPE_{AB} \approx ZPE_A + ZPE_B$, so that for dissociation reactions $\Delta ZPE \approx 0$ and $\Delta H_{Diss} \approx \Delta E_{Diss}$. For $*CH_3OH$ at NiO_2(110), ZPE_{CH_3OH}, ZPE_{OH} and ZPE_{CH_3} are 1.42, 0.38 and 0.97 eV. Thus, ΔZPE = 0.07 eV, which is negligible considering the accuracy of DFT and BEP relations. Besides, the ZPEs do not appreciably change among rutile oxides: ZPE_{CH_3OH} is 1.42 eV on both NiO_2(110) and TiO_2(110). Thus, including ZPEs will not sizably affect the BEP relations reported here. In this order of ideas, the reaction energy (ΔH_{Diss}) of elementary reactions was approximated as:

$$\Delta H_{Diss} \approx \Delta E_{Diss} = E_{FS} - E_{IS} \quad (2)$$

where E_{FS} and E_{IS} are the energy of the most stable configurations for the adsorption of the intermediates in the final state (E_{FS}) and initial state (E_{IS}). For example, for CH_3OH scission the initial state is adsorbed $*CH_3OH$, and the final state is $*CH_3$ + *OH.

All transition states (TSs) were located by the force reversed method[54] and the climbing-image nudged elastic band method (CI-NEB)[55] and confirmed by vibrational frequency analysis. The relaxations stopped when the residual forces on each atom were smaller than 0.03 eV Å^{-1}. The elementary activation barrier (ΔE_{Act}) was calculated using the TS (E_{TS}) with respect to the most stable configurations for the adsorption of species at the IS (E_{IS}):

$$\Delta E_{Act} = E_{TS} - E_{IS} \quad (3)$$

The formation energy of a surface oxygen vacancy (ΔE_{Vac}) is:

$$\Delta E_{Vac} = \frac{1}{2}E_{O_2} + E_{MO_{2-v}} - E_{MO_2} \quad (4)$$

where $\frac{1}{2}E_{O_2}$, $E_{MO_{2-\nu}}$ and E_{MO_2} are half the energy of molecular oxygen and the energies of the defective and pristine rutile slabs, respectively. We calculated $\frac{1}{2}E_{O_2}$ using the DFT-assessed free energies of H_2 and H_2O and the experimental free energy change of the reaction $H_2O \rightarrow \frac{1}{2}O_2 + H_2$, which is 2.46 eV. This is done to avoid the direct calculation of the total energy of O_2,[56,57] which is generally problematic within the DFT formalism.[58] All the adsorption, reaction, activation, and vacancy formation energies are found in Tables S3–S5.†

We note that some oxides such as CoO_2 and NiO_2 may not exhibit the rutile phase under catalytic conditions. However, this does not affect the main purpose of this work, which is the identification and description of general reactivity trends for an important family of oxides.

3. Results and discussion

As shown in Fig. 1a, there is a linear Brønsted–Evans–Polanyi (BEP)-type relationship[59] between activation energies (ΔE_{Act}) and reaction energies (ΔE_{Diss}) for CO_2, CH_3OH, N_2O and NH_2OH dissociation (see the reactions in Fig. 1a) at the bridge oxygen vacancy on the rutile (110) surfaces. This suggests that scission kinetics and thermodynamics are proportional and well correlated in this case.

Compared to CO_2 and CH_3OH decomposition (-0.51 eV $\leq \Delta E_{Diss} \leq 3.19$ eV; 0.62 eV $\leq \Delta E_{Act} \leq 3.23$ eV), N_2O and NH_2OH decomposition is generally more exothermic (-3.80 eV $\leq \Delta E_{Diss} \leq 0.23$ eV), and the corresponding ΔE_{Act} values are lower, falling in the range of 0.13–1.25 eV (see Table S3† for the specific values). A good relationship is also observed for CO_2, N_2O and NH_2OH dissociation barriers and the transition-state geometries, represented by N–O or C–O bond lengths (d in Fig. 1b and Table S3†). Briefly, the shorter the N–O or C–O bond length at the TS, the lower the barrier, which agrees well with previous DFT study results for CO oxidation on metals and metal oxides.[18,60]

Identifying a BEP relationship enables relatively fast assessment of catalytic activities by using the reaction energy ΔE_{Diss} as a descriptor for trends in transition-state (TS) barriers. Nevertheless, we note that calculating ΔE_{Diss}, which involves both initial (IS) and final (FS) states (eqn (2)), is still a demanding task when dealing with a great number of systems and/or large unit cells. In the following, we will show that more affordable and experimentally available descriptors exist.

In Fig. 2 we plot the adsorption energies ΔE_{Ads} of CO_2, CH_3OH, N_2O and NH_2OH and their cleaved moieties against ΔE_{Diss}. Fig. 2 and Table S4† show that the ISs for CO_2, CH_3OH, N_2O and NH_2OH decomposition are almost independent of the chemical nature of the element M in MO_2. To illustrate this, consider the case of CO_2: the adsorption energies (ΔE_{Ads}) vary only by ~0.25 eV on the bridge oxygen vacancy of the analyzed rutile surfaces, but ΔE_{Diss} changes by ~3.7 eV (see the values in Tables S3 and S4† and the structures in Fig. S3†).

The results in Fig. 2 suggest that, as the adsorption energies of initial states (ISs) are nearly constant, the trends in ΔE_{Diss} (eqn (2)) are mainly determined by the final states (FSs).

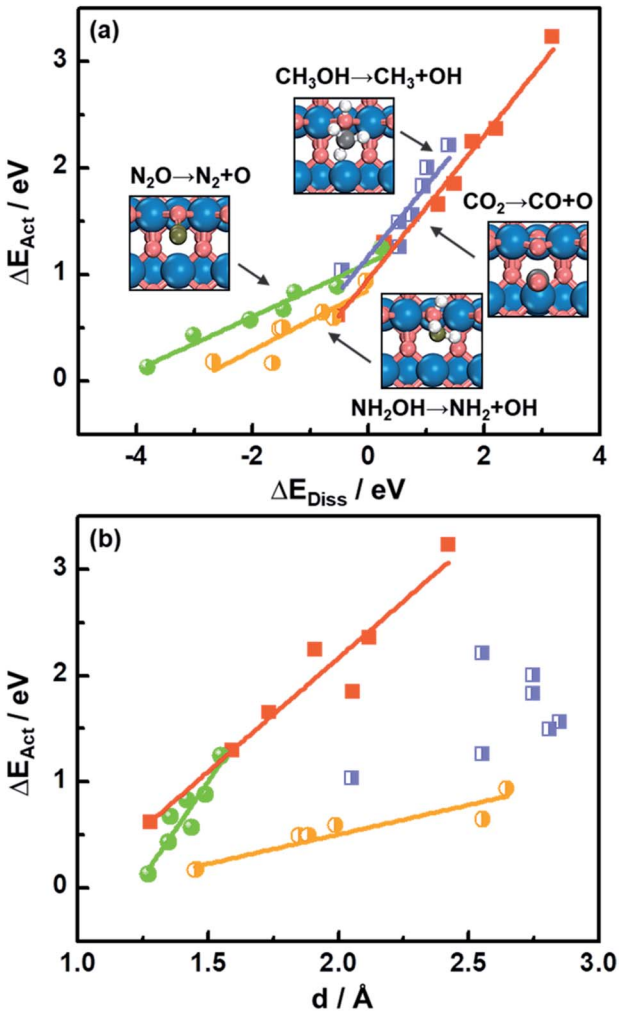

Fig. 1 Activation energies (ΔE_{Act}) for C–O and N–O bond scissions as a function of (a) reaction energies (ΔE_{Diss}) and (b) the C–O or N–O distances (d) at the transition states on rutile MO_2(110) surfaces. Insets: transition-state structures for C–O and N–O bond scission. Blue, vermilion, grey, ochre and white balls represent 3d metals (Ti–Ni) and O, C, N and H atoms, respectively.

The downward shift of the FS curve can lead to more negative ΔE_{Diss} and to the shift of the reaction coordinate of the transition state closer to the ISs.[59] This explains the relationship between ΔE_{Act} and N–O or C–O bond distance d at the TSs in Fig. 1b well. The deviation from the linear trend of ΔE_{Act} *vs.* d in the case of CH_3OH dissociation is justified by the surface reconstruction of CoO_2(110) and NiO_2(110).

Compared to the trivial molecular adsorption at the ISs shown in Fig. 2 and Table S4,† the trends in dissociative adsorption, *i.e.* the FSs, are slightly more elaborate. We have identified two groups in the trends: (1) intermediates such as *CO, *N_2 and *CH_3 adsorbed at the coordinatively unsaturated 3d metals on the FSs do not exhibit strong dependence on the chemical nature of M (Fig. S3b, e and g†). (2) *O, *OH and *NH_2 adsorption at the bridge oxygen vacancy and coordinatively unsaturated 3d metals on the FSs are oxide-dependent (Fig. S3c, h and j†), with the largest differences in ΔE_{Ads} being 4.10, 1.98 and 1.25 eV, respectively (see Table S4†).

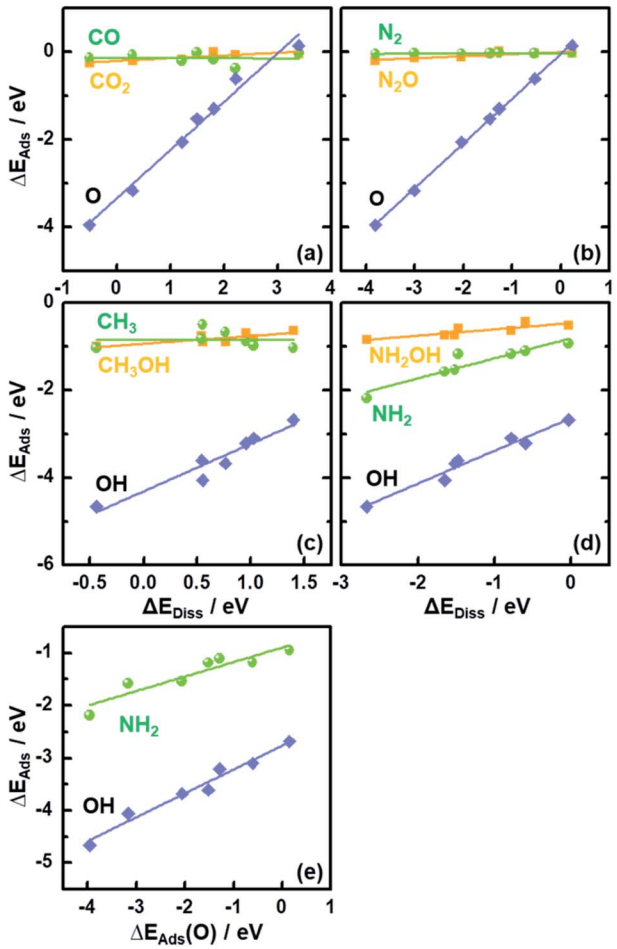

Fig. 2 Adsorption energies (ΔE_{Ads}) of reactants and products of C–O bond scission for (a) CO_2 and (c) CH_3OH and N–O bond scission for (b) N_2O and (d) NH_2OH plotted as a function of the reaction energies (ΔE_{Diss}) on MO_2(110). (e) ΔE_{Ads} of NH_2 and OH plotted against that of O.

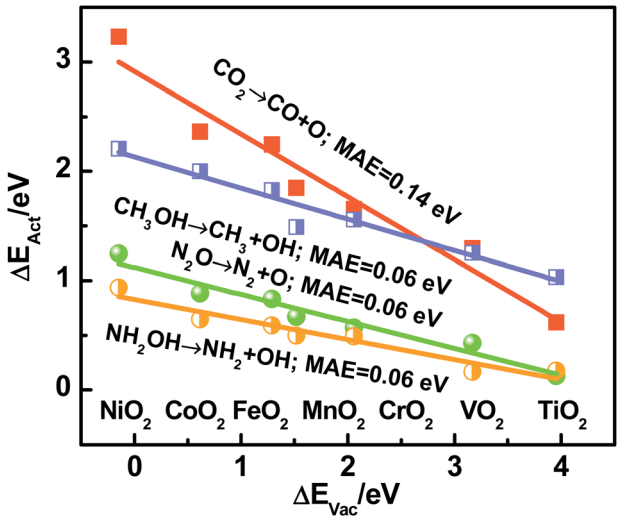

Fig. 3 Activation energy (ΔE_{Act}) for C–O and N–O bond scissions plotted as a function of the vacancy formation energy (ΔE_{Vac}) on MO_2(110). The analyzed oxides are respectively marked in the trends. MAE: mean absolute error.

Since ΔE_{Ads}(OH) and ΔE_{Ads}(NH_2) scale linearly with ΔE_{Ads}(O), as shown in Fig. 2e, the trends in ΔE_{Diss} for the C–O and N–O bond scission reactions are modulated by a single metal-dependent parameter, namely ΔE_{Ads}(O). Since creating an oxygen vacancy is the reverse process of oxygen adsorption at such a vacancy, we have: $\Delta E_{Ads}(O) = -\Delta E_{Vac}$, see eqn (1) and (4). This is important, as ΔE_{Vac} is a common parameter for oxide systems.

Recapitulating, transition-state energies and reaction energies are connected through a linear BEP relation ($\Delta E_{Act} = \gamma + \phi\Delta E_{Diss}$, see Fig. 1a), and reaction energies and the O adsorption energies are in turn connected ($\Delta E_{Diss} = \varepsilon + \delta\Delta E_{Ads}(O)$, see Fig. 2). Since ΔE_{Ads}(O) is the additive inverse of ΔE_{Vac}, one can expect the following, where α and β depend on the specific dissociation reaction:

$$\Delta E_{Act} = \alpha - \beta\Delta E_{Vac} \quad (5)$$

This is exactly what we observe in Fig. 3, where ΔE_{Act} correlates well with ΔE_{Vac} for all oxides and reactions considered in this study, in all cases with a negative slope. The linear relationships between ΔE_{Act} and ΔE_{Vac} found for all the C–O and N–O bond scission reactions indicate that ΔE_{Vac} can be used as a single descriptor to analyze a number of dissociation reactions on rutile surfaces. According to Fig. 3, as ΔE_{Vac} increases from NiO_2 to TiO_2, ΔE_{Act} gradually decreases, which suggests that strengthening bridge oxygen–metal bonds can significantly promote C–O and N–O bond scission reactions.

To further understand the nature of the bond between bridge oxygen and metal ions in rutile oxides, we calculated in Fig. 4 the differential charge density maps. It can be seen from Fig. 4a that there is considerable charge withdrawal from Ti by O in TiO_2, which is indicative of rather ionic bonds. Fig. 4b–d show sizeable charge depletion from both M (M = Cr, Fe and Ni) and O centers and accumulation between them, meaning that the bonds are covalent. Furthermore, the charge withdrawn from O (blue part) gradually increases when moving from CrO_2 to NiO_2, suggesting that more and more electrons contribute to the formation of the bond and lead to stronger covalent interactions. Therefore, these results show that the bridge oxygen–metal bond switches from ionic to covalent when moving from TiO_2 to NiO_2, which is in turn responsible for the decrease in ΔE_{Vac}.

In contrast, for N_2O adsorption at the bridge O vacancy, we find charge depletion from metal centers and O centers in N_2O and accumulation between them for all the rutile oxides studied, as shown in Fig. 4e–h, indicating that the bonds are covalent. Interestingly, the distance between M and O in N_2O is closely related to the charge transferred. As the M–O distance increases from TiO_2 and CrO_2 (~2.5 Å) to FeO_2 and NiO_2 (~3.0 Å), the charge transferred markedly decreases. The similar bond nature between M and N_2O also leads to a small variation in adsorption energies of 0.22 eV only. We note that this explanation based on bond ionicity and covalency is similar to that in previous studies on metalloporphyrins[61] and metals,[7] which grants generality to the analysis.

In brief, Fig. 2–4 show that reaction energies (ΔE_{Diss}), activation energies (ΔE_{Act}), oxygen vacancy formation energies

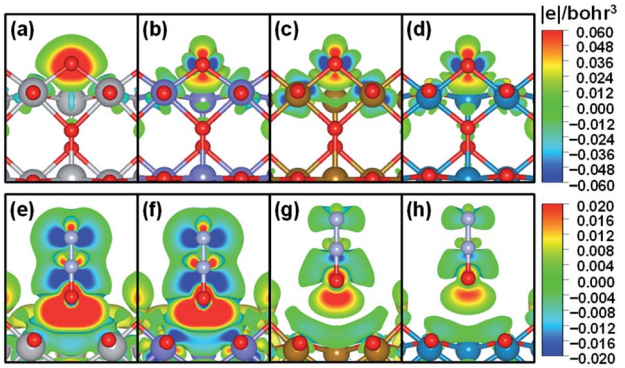

Fig. 4 Differential charge density map for adsorption of O (upper panels) and N_2O (lower panels) at the bridge O vacancy on MO_2(110). (a and e) M = Ti; (b and f) M = Cr; (c and g) M = Fe; (d and h) M = Ni. Grey, purple, orange, green, red and light purple spheres represent Ti, Cr, Fe, Ni, O and N, respectively. Blue and yellow-red isosurfaces indicate charge depletion and accumulation, respectively. The 2D profile is a cut along two bridge O–M bonds.

(ΔE_{Vac}), and electronic charges are all connected on rutile oxides, which holds promise for understanding and rationally capitalizing on the high activity of oxygen vacancies at rutile oxides observed experimentally.

We emphasize that ΔE_{Vac} is a more convenient descriptor than the others analyzed here in view of its straightforward calculation and experimental measurability.

4. Conclusions

By adsorbing and cleaving CO_2, CH_3OH, N_2O, and NH_2OH, we were able to construct linear BEP relationships for C–O and N–O bond scissions taking place at oxygen vacancies on rutile oxides. Interestingly, the analysis of the trends allowed us to identify the oxygen vacancy formation energy as a simple yet accurate descriptor for the transition-state energies of such scissions. This is important because oxygen vacancy formation energies are more easily calculated than transition-state energies and can be measured experimentally.

The nature of the bond between bridge oxygen and 3d metals in rutile oxides changes from ionic to covalent when moving from the left to the right of the periodic table (Ti to Ni), in line with the trends in formation energies of surface oxygen vacancies. The insight gained from this study can be used to enrich the design principles for oxide catalysts and simplify their modelling, particularly for those where lattice oxygen and/or oxygen vacancies participate in the catalytic cycles.

Conflicts of interest

There are no conflicts to declare.

Acknowledgements

We gratefully acknowledge the financial support from the Natural Science Foundation of China (21872136 and 21603146), the Ministry of Science and Technology of China (2017YFA0204800), the Guangdong Innovation Research Team for Higher Education (2017KCXTD030) and the High-level Talents Project of the Dongguan University of Technology (KCYKYQD2017017). We also received funding from the Engineering Research Center of None-food Biomass Efficient Pyrolysis and Utilization Technology of Guangdong Higher Education Institutes (grant 2016GCZX009). F. C. V. acknowledges funding from the Spanish MICIUN through a Ramón y Cajal research contract (RYC-2015-18996) and the program "Units of Excellence María de Maeztu" (grant MDM-2017-0767) and Generalitat de Catalunya (project 2017SGR13). We thank Red Española de Supercomputación (RES) for supercomputing time at SCAYLE (projects QS-2019-3-0018, QS-2019-2-0023, and QCM-2019-1-0034). The use of the supercomputing facilities at SURFsara was sponsored by NWO Physical Sciences, with financial support from the NWO.

References

1 B. Hammer and J. K. Nørskov, *Adv. Catal.*, 2000, **45**, 71–129.
2 J. K. Nørskov, F. Abild-Pedersen, F. Studt and T. Bligaard, *Proc. Natl. Acad. Sci. U. S. A.*, 2011, **108**, 937–943.
3 R. A. Van Santen, *Acc. Chem. Res.*, 2009, **42**, 57–66.
4 J. K. Nørskov, T. Bligaard, J. Rossmeisl and C. H. Christensen, *Nat. Chem.*, 2009, **1**, 37–46.
5 F. Calle-Vallejo, J. I. Martinez, J. M. Garcia-Lastra, P. Sautet and D. Loffreda, *Angew. Chem., Int. Ed.*, 2014, **53**, 8316–8319.
6 X. Ma and H. Xin, *Phys. Rev. Lett.*, 2017, **118**, 036101.
7 H.-Y. Su, K. Sun, W.-Q. Wang, Z. H. Zeng, F. Calle-Vallejo and W.-X. Li, *J. Phys. Chem. Lett.*, 2016, **7**, 5302–5306.
8 C. D. Gelatt, A. R. Williams and V. L. Moruzzi, *Phys. Rev. B: Condens. Matter Mater. Phys.*, 1983, **27**, 2005–2013.
9 J. F. Weaver, *Chem. Rev.*, 2013, **113**, 4164–4215.
10 J. Suntivich, K. J. May, H. A. Gasteiger, J. B. Goodenough and Y. Shao-Horn, *Science*, 2011, **334**, 1383–1385.
11 F. Calle-Vallejo, N. G. Inoglu, H.-Y. Su, J. I. Martinez, I. C. Man, M. T. M. Koper, J. R. Kitchin and J. Rossmeisl, *Chem. Sci.*, 2013, **4**, 1245–1249.
12 V. Fung, F. F. Tao and D.-e. Jiang, *J. Phys. Chem. Lett.*, 2017, **8**, 2206–2211.
13 Y. L. Lee, J. Kleis, J. Rossmeisl, Y. Shao-Horn and D. J. E. Morgan, *Energy Environ. Sci.*, 2011, **4**, 3966–3970.
14 C. F. Dickens, J. H. Montoya, A. R. Kulkarni, M. Bajdich and J. K. Nørskov, *Surf. Sci.*, 2019, **681**, 122–129.
15 Y. Hinuma, T. Toyao, T. Kamachi, Z. Maeno, S. Takakusagi, S. Furukawa, I. Takigawa and K. Shimizu, *J. Phys. Chem. C*, 2018, **122**, 29435–29444.
16 S. Wang, V. Petzold, V. Tripkovic, J. Kleis, J. G. Howalt, E. Skúlason, E. M. Fernández, B. Hvolbæk, G. Jones, A. Toftelund, H. Falsig, M. Björketun, F. Studt, F. Abild-Pedersen, J. Rossmeisl, J. K. Nørskov and T. Bligaard, *Phys. Chem. Chem. Phys.*, 2011, **13**, 20760–20765.
17 S. Wang, B. Temel, J. Shen, G. Jones, L. C. Grabow, F. Studt, T. Bligaard, F. Abild-Pedersen, C. H. Christensen and J. K. Nørskov, *Catal. Lett.*, 2011, **141**, 370–373.
18 A. Vojvodic, F. Calle-Vallejo, W. Guo, S. Wang, A. Toftelund, F. Studt, J. I. Martinez, J. Shen, I. C. Man, J. Rossmeisl,

T. Bligaard, J. K. Nørskov and F. Abild-Pedersen, *J. Chem. Phys.*, 2011, **134**, 244509.
19 A. L. Linsebigler, G. Lu and J. T. Yates, *Chem. Rev.*, 1995, **95**, 735–758.
20 A. Fujishima and K. Honda, *Nature*, 1972, **238**, 37–38.
21 M. Haruta, *Cattech*, 2002, **6**, 102–115.
22 J. Huusko, V. Lantto and H. Torvela, *Sens. Actuators, B*, 1993, **15**, 245–248.
23 G. Pacchioni, *ChemPhysChem*, 2003, **4**, 1041–1047.
24 J. A. Rodriguez, S. Ma, P. Liu, J. Hrbek, J. Evans and M. Perez, *Science*, 2007, **318**, 1757–1760.
25 R. Schaub, P. Thostrup, N. Lopez, E. Laegsgaard, I. Stensgaard, J. K. Nørskov and F. Besenbacher, *Phys. Rev. Lett.*, 2001, **87**, 266104.
26 Y. G. Wang, Y. Yoon, V. A. Glezakou, J. Li and R. Rousseau, *J. Am. Chem. Soc.*, 2013, **135**, 10673–10683.
27 X. Wu, A. Selloni and S. K. Nayak, *J. Chem. Phys.*, 2004, **120**, 4512–4516.
28 M. Al-Hashem, S. Akbar and P. Morris, *Sens. Actuators, B*, 2019, **301**, 126845.
29 C. T. Campbell and C. H. F. Peden, *Science*, 2005, **309**, 713–714.
30 Y. Matsumoto and E. Sato, *Mater. Chem. Phys.*, 1986, **14**, 397–426.
31 J. G. Vos, T. A. Wezendonk, A. W. Jeremiasse and M. T. M. Koper, *J. Am. Chem. Soc.*, 2018, **140**, 10270–10281.
32 H. Over, *Science*, 2000, **287**, 1474–1476.
33 R. Mu, D. C. Cantu, X. Lin, V.-A. Glezakou, Z. Wang, I. Lyubinetsky, R. Rousseau and Z. Dohnalek, *J. Phys. Chem. Lett.*, 2014, **5**, 3445–3450.
34 Y. Bian, M. Kim, T. Li, A. Asthagiri and J. F. Weaver, *J. Am. Chem. Soc.*, 2018, **140**, 2665–2672.
35 C.-H. Yeh, P. Thong Minh Le, S. Nachimuthu and J.-C. Jiang, *ACS Catal.*, 2019, **9**, 8230–8242.
36 O. Diaz-Morales, F. Calle-Vallejo, C. de Munck and M. T. M. Koper, *Chem. Sci.*, 2013, **4**, 2334–2343.
37 A. Grimaud, O. Diaz-Morales, B. Han, W. T. Hong, Y.-L. Lee, L. Giordano, K. A. Stoerzinger, M. T. M. Koper and Y. Shao-Horn, *Nat. Chem.*, 2017, **9**, 457–465.
38 N. B. Halck, V. Petrykin, P. Krtil and J. Rossmeisl, *Phys. Chem. Chem. Phys.*, 2014, **16**, 13682–13688.
39 M. Retuerto, F. Calle-Vallejo, L. Pascual, P. Ferrer, A. Garcia, J. Torrero, D. Gianolio, J. L. G. Fierro, M. A. Pena, J. Antonio Alonso and S. Rojas, *J. Power Sources*, 2018, **404**, 56–63.
40 F. Cheng, T. Zhang, Y. Zhang, J. Du, X. Han and J. Chen, *Angew. Chem., Int. Ed.*, 2013, **52**, 2474–2477.
41 D. A. Tompsett, S. C. Parker and M. S. Islam, *J. Am. Chem. Soc.*, 2014, **136**, 1418–1426.
42 C. Doornkamp and V. Ponec, *J. Mol. Catal. A: Chem.*, 2000, **162**, 19–32.
43 L. Xue, C. B. Zhang, H. He and Y. Teraok, *Appl. Catal., B*, 2007, **75**, 167–174.
44 J. H. Wu, Y. Huang, W. Ye and Y. G. Li, *Adv. Sci.*, 2017, **4**, 1700194.
45 Y. Y. Birdja, E. Pérez-Gallent, M. C. Figueiredo, A. J. Göttle, F. Calle-Vallejo and M. T. M. Koper, *Nat. Energy*, 2019, **4**, 732–745.
46 K. Drew, G. Girishkumar, K. Vinodgopal and P. V. Kamat, *J. Phys. Chem. B*, 2005, **109**, 11851–11857.
47 V. Rosca, G. L. Beltramo and M. T. M. Koper, *J. Electroanal. Chem.*, 2004, **566**, 53–62.
48 C. T. Campbell and J. R. V. Sellers, *Chem. Rev.*, 2013, **113**, 4106–4135.
49 G. Kresse and J. Furthmüller, *Phys. Rev. B: Condens. Matter Mater. Phys.*, 1996, **54**, 11169–11186.
50 J. P. Perdew, K. Burke and M. Ernzerhof, *Phys. Rev. Lett.*, 1996, **77**, 3865–3868.
51 P. E. Blöchl, *Phys. Rev. B: Condens. Matter Mater. Phys.*, 1994, **50**, 17953–17979.
52 H. J. Monkhorst, *Phys. Rev. B: Condens. Matter Mater. Phys.*, 1976, **16**, 1748–1749.
53 S. Grimme, J. Antony, S. Ehrlich and H. Krieg, *J. Chem. Phys.*, 2010, **132**, 154104.
54 K. J. Sun, Y. H. Zhao, H.-Y. Su and W.-X. Li, *Theor. Chem. Acc.*, 2012, **131**, 1118.
55 G. Henkelman, *J. Chem. Phys.*, 2000, **113**, 9978–9985.
56 J. I. Martinez, H. A. Hansen, J. Rossmeisl and J. K. Nørskov, *Phys. Rev. B: Condens. Matter Mater. Phys.*, 2009, **79**, 045120.
57 F. Calle-Vallejo, J. I. Martinez, J. M. Garcia-Lastra, M. Mogensen and J. Rossmeisl, *Angew. Chem., Int. Ed.*, 2010, **49**, 7699–7701.
58 S. Kurth, J. P. Perdew and P. Blaha, *Int. J. Quantum Chem.*, 1999, **75**, 889–909.
59 M. G. Evans and M. Polanyi, *Trans. Faraday Soc.*, 1938, **34**, 11–24.
60 X. Q. Gong, Z. P. Liu, R. Raval and P. Hu, *J. Am. Chem. Soc.*, 2004, **126**, 8–9.
61 F. Calle-Vallejo, A. Krabbe and J. M. Garcia-Lastra, *Chem. Sci.*, 2017, **8**, 124–130.